Green Chemical Technology

SCIEPublish

Article

Zr-Doped Ru-Based Catalyst for Highly Active and Durable Acidic Oxygen Evolution Reaction

Ju Zhang [1,2], Junli Wang [3], Ruidong Xu [1,2,*] and Xuanbing Wang [1,2,*]

[1] State Key Laboratory of Complex Nonferrous Metal Resources Clean Utilization, Kunming University of Science and Technology, Kunming 650093, China; zjkust@stu.kust.edu.cn (J.Z.)

[2] Faculty of Metallurgical and Energy Engineering, Kunming University of Science and Technology, Kunming 650093, China

[3] Researcher Center for Analysis and Measurement, Kunming University of Science and Technology, Kunming 650093, China; 20070141@kust.edu.cn (J.W.)

* Corresponding author. E-mail: rdxupaper@kust.edu.cn (R.X.); xuanbingwang@kust.edu.cn (X.W.)

Received: 23 February 2026; Revised: 16 March 2026; Accepted: 9 April 2026; Available online: 20 April 2026

ABSTRACT: Developing an oxygen evolution reaction catalyst that exhibits both high catalytic activity and robust stability in acidic media remains a significant challenge to date. In this work, a $RuZrO_x$/Ti-1 catalyst was successfully constructed on a Ti mesh substrate via a facile one-step pyrolysis method. Physical characterization reveals that the as-prepared $RuZrO_x$/Ti-1 catalyst exhibits a densely packed nanosphere morphology on its surface, accompanied by abundant pores, which can provide a rich interface for the oxygen evolution reaction. The $RuZrO_x$/Ti-1 catalyst achieves a low overpotential of only 199 mV for the OER at a current density of 10 $mA \cdot cm^{-2}$ and demonstrates excellent long-term durability, operating stably for 400 h at this current density. In summary, this work provides a viable strategy for designing high-performance acidic OER catalysts, thereby paving the way for the advancement of electrodes for water oxidation.

Keywords: Acidic oxygen evolution reaction (OER); Zr doping; Ru-based electrocatalyst

1. Introduction

The escalating environmental pollution caused by traditional energy sources (such as coal, oil, and natural gas) has accelerated the development and adoption of clean and renewable energy alternatives [1–3]. For proton exchange membrane water electrolysis—a technology capable of producing green hydrogen with high durability and high current density—the anodic oxygen evolution reaction plays a decisive role in determining the energy conversion efficiency [4–6]. However, most OER catalysts exhibit low OER kinetics and unsatisfactory stability in acidic environments [7–10]. Iridium-based materials are regarded as the state-of-the-art catalysts for the OER; nevertheless, their prohibitively high cost poses a significant barrier to commercial expansion [11,12]. In contrast, ruthenium-based catalysts have emerged as promising alternatives for PEM water electrolysis due to their lower cost and outstanding OER activity under acidic conditions [13–15]. However, pristine RuO_2 catalysts still suffer from instability in acidic electrolytes. Overoxidation issues and the participation of lattice oxygen in the reaction lead to the rupture and reformation of Ru–O bonds, ultimately resulting in the deactivation of RuO_2 catalysts [16,17]. Therefore,

the development of highly active and stable ruthenium-based anodic catalysts is crucial for advancing acidic water electrolysis technology.

Based on existing research, the performance enhancement of Ru-based catalysts primarily focuses on two strategies: the first involves enhancing the intrinsic activity of catalytic materials through the introduction of defect engineering (such as oxygen vacancies), heterojunctions, and lattice distortion; the second strategy entails introducing metal elements with weaker electronegativity than Ru to lower the oxidation state of Ru via doping and inhibit its overoxidation during the OER, thereby enhancing the stability of the catalytic material [18–20]. Regarding the selection of dopant elements, this study comprehensively considered the electronic structure, lattice matching, and stability in acidic electrolytes. First, elements with lower electronegativity were screened, as they are favorable for donating electrons to Ru, thereby weakening Ru–O covalency. Furthermore, considering that the Ru-based active species in the catalyst ultimately form RuO_2 dominated by Ru^{4+}, titanium-group elements (e.g., Ti, Hf, Zr) that exist in the +4 oxidation state were selected to preserve the structural integrity as much as possible. This isovalent substitution mitigates charge imbalance and lattice distortion caused by heterovalent doping. Second, M^{4+} ions possess an empty d-orbital configuration, endowing their corresponding oxides with excellent acid corrosion resistance and thermal stability—key characteristics required for an efficient acidic OER catalyst. Finally, to synergistically enhance both the catalytic activity and stability of the material, Zr was chosen as the dopant metal because it has a lower electronegativity than Ti while being less expensive than Hf [21,22]. The introduction of Zr ions can provide additional electrons to the Ru centers, stabilize their valence state, and prevent the overoxidation of Ru that leads to the formation of soluble high-valent ruthenium oxides. Additionally, the differing ionic radii between Zr and Ru ions may induce controllable lattice distortion, optimizing the electronic structure of Ru sites within the catalyst and their adsorption energy for oxygen-containing intermediates [23–25]. In this study, Ru and Zr precursors were loaded onto pretreated Ti mesh surfaces using a drop-coating method, followed by a one-step pyrolysis process under a nitrogen atmosphere to synthesize a Zr-doped RuO_2 nanosphere composite catalyst for the OER under acidic conditions (hereinafter referred to as $RuZrO_x$/Ti). Benefiting from the introduction of the new metal element Zr, the $RuZrO_x$/Ti nanosphere catalyst exhibits overpotentials of 199 mV, 382 mV, and 512 mV at current densities of 10 $mA \cdot cm^{-2}$, 50 $mA \cdot cm^{-2}$, and 100 $mA \cdot cm^{-2}$, respectively. Furthermore, the $RuZrO_x$/Ti nanosphere catalyst can operate stably for 400 h at a current density of 100 $mA \cdot cm^{-2}$. In addition, *in situ* Raman spectroscopy indicates that $RuZrO_x$/Ti does not undergo significant irreversible degradation or overoxidation during the OER process. Therefore, this study introduces a strategy through doping engineering to enhance catalyst activity and stability, providing an additional option for the synthesis of OER catalysts in acidic environments.

2. Materials and Methods

2.1. Materials

Ruthenium(III) chloride trihydrate ($RuCl_3 \cdot 3H_2O$) and zirconium(IV) nitrate pentahydrate ($Zr(NO_3)_4 \cdot 5H_2O$) were purchased from Aladdin Industrial Corporation (Shanghai, China). Ethanol (C_2H_6O) was obtained from Tianjin Kemiou Chemical Reagent Co., Ltd. (Tianjin, China). Titanium mesh (Ti mesh) was supplied by Kunshan Hengbo New Materials Co., Ltd. (Kunshan, China). All chemical reagents were of analytical grade and used as received without further purification.

2.2. Fabrication of $RuZrO_x$/Ti

In this study, a facile synthesis strategy was employed to successfully fabricate $RuZrO_x$/Ti nanosphere composite catalysts via a drop-coating method followed by one-step pyrolysis on pretreated Ti mesh substrates. First, the Ti mesh was etched using a mixed solution of hydrofluoric acid, nitric acid, and

deionized water in a volume ratio of 1:1:2 to remove the natural oxide layer and surface contaminants, thereby exposing the pristine Ti surface and increasing the surface roughness. This treatment optimized the interfacial bonding strength between the active material and the Ti mesh substrate, enhancing the stability of the active material loading process [26]. Subsequently, 0.3 mmol of $RuCl_3 \cdot 3H_2O$ and 0.008 mmol of $Zr(NO_3)_4 \cdot 5H_2O$ (As shown in Figure S1, the LSV curves of the samples at different molar ratios indicate that this molar ratio has been verified as the optimal one) were dissolved in 20 mL of a mixed solution consisting of anhydrous ethanol and deionized water in a volume ratio of 9:1. The thoroughly mixed solution was drop-coated onto the Ti mesh surface to obtain the precursor samples (The average loading mass of the active substance is between 0.2 mg and 0.3 mg), which were then placed in a vacuum drying oven for subsequent use. The precursor samples were subjected to pyrolysis treatment at 400 °C for 4 h in two different atmospheres: one in a quartz tube under a N_2 flow, and the other in a muffle furnace under ambient air. Finally, the catalyst obtained from pyrolysis under N_2 atmosphere was denoted as $RuZrO_x$/Ti-1, while the catalyst obtained from pyrolysis under air atmosphere was denoted as $RuZrO_x$/Ti-2.

2.3. Characterizations

The micromorphology and elemental distribution of the samples were characterized using scanning electron microscopy (SEM) with a Nova Nano SEM 450 instrument (FEI, Hillsboro, OR, USA). The chemical composition and valence states of the samples were analyzed by X-ray diffraction (XRD) and X-ray photoelectron spectroscopy (XPS), respectively. XRD patterns were obtained using a D/max 2200 diffractometer (Rigaku Corporation, Tokyo, Japan) with Cu-Kα radiation, while XPS measurements were performed on a PHI 5500 spectrometer (ULVAC-PHI, Chigasaki, Japan). Raman spectroscopy was employed to monitor the evolution of chemical bonds during the OER process using a LabRam Odyssey Raman spectrometer (Horiba Scientific, Tokyo, Japan).

2.4. Electrochemical Measurement

Electrochemical measurements were performed using a standard three-electrode configuration. In this system, the as-prepared catalyst samples served as the working electrode, a carbon rod was used as the counter electrode, and a saturated calomel electrode (SCE) functioned as the reference electrode. The electrolyte was 0.5 M H_2SO_4 solution (pH ≈ 0). All potentials measured against the SCE were converted to the reversible hydrogen electrode (RHE) scale according to the equation: $E_{RHE} = E_{SCE} + 0.242 + 0.0591\ pH$.

Linear sweep voltammetry (LSV) curves were recorded at a scan rate of 5 $mV \cdot s^{-1}$. The overpotential values reported in this study were obtained directly from the LSV curves without iR compensation. The stability of the oxygen evolution reaction (OER) was evaluated at a fixed current density of 10 $mA \cdot cm^{-2}$. To determine the double-layer capacitance (C_{dl}), cyclic voltammetry (CV) curves were collected in the non-Faradaic potential region at scan rates of 20, 40, 60, 80, and 100 $mV \cdot s^{-1}$. The C_{dl} value was calculated using the equation $1/2 \times \Delta j = \nu \times C_{dl}$, where Δj represents the current density difference obtained from the CV curves, and ν is the scan rate. The electrochemical surface area (ECSA) is proportional to the double-layer capacitance and was quantitatively determined using the formula $ECSA = C_{dl}/C_s$. In this study, the specific capacitance (C_s) was taken as 0.04 $mF \cdot cm^{-2}$, a commonly reported value in the literature [27,28]. Electrochemical impedance spectroscopy (EIS) Nyquist plots were recorded over a frequency range of 100,000 Hz to 0.1 Hz.

3. Results and Discussion

The preparation process of the $RuZrO_x$/Ti catalyst is illustrated in Figure 1. The precursor solution was drop-coated onto the Ti mesh surface, followed by a one-step pyrolysis method to successfully synthesize a self-supporting acidic OER electrocatalytic electrode. To investigate the morphological characteristics of the catalyst material, SEM images of $RuZrO_x$/Ti-1 were collected (Figure 2a,b). Observation of the low-

magnification SEM image (Figure 2a) reveals that the active material is uniformly adhered to the surface of the Ti mesh framework. At higher magnification (Figure 2b), it can be observed that $RuZrO_x$ exhibits a nanosphere morphology (The particle size distribution graph is shown in Figure S2), and within this uniformly distributed and dense nanosphere arrangement, numerous pore structures are also present. This spherical and porous surface facilitates more sufficient contact between the active material and the electrolyte, thereby enhancing the OER performance. Furthermore, EDS mapping analysis was conducted on the $RuZrO_x$/Ti-1 material to verify the elemental distribution on the material surface. From Figure 2c–f, it can be observed that four elements—Ti, Ru, Zr, and O—are present within the catalytic material, and no element enrichment phenomenon was observed, indicating that $RuZrO_x$ is uniformly loaded on the Ti mesh surface.

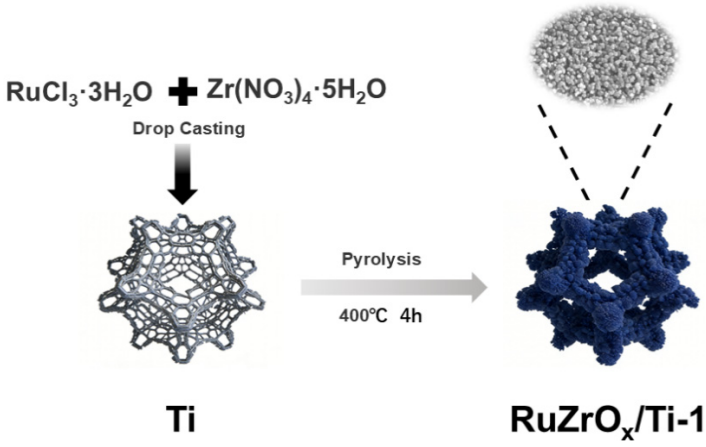

Figure 1. Schematic illustration of the synthesis process for $RuZrO_x$/Ti-1.

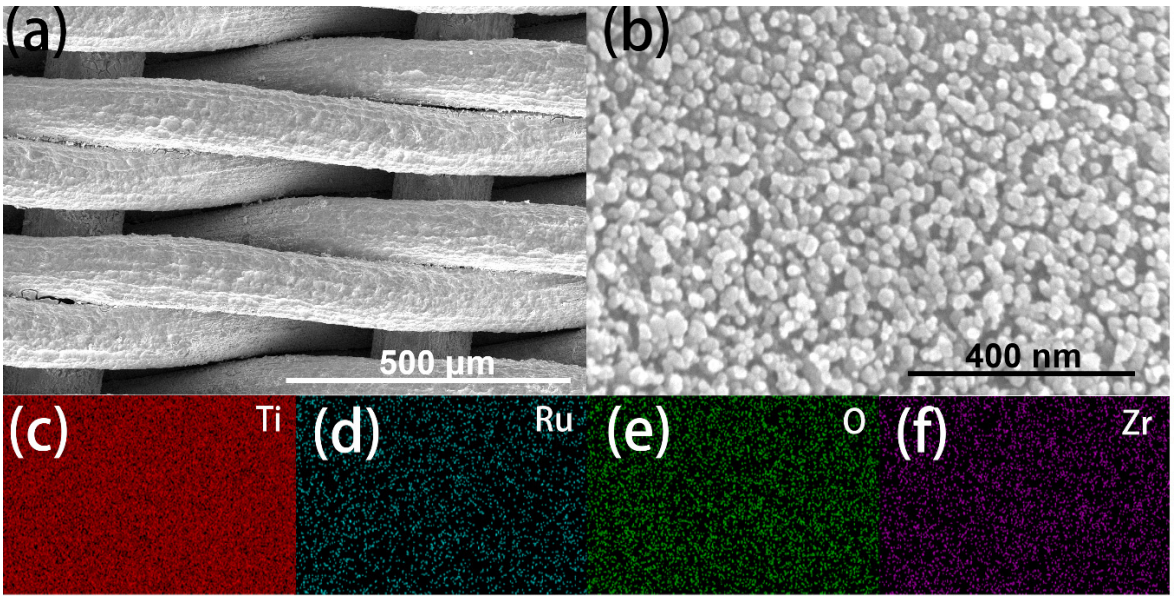

Figure 2. (**a**) Low-magnification SEM image of $RuZrO_x$/Ti-1; (**b**) High-magnification SEM image of $RuZrO_x$/Ti-1; EDS elemental mapping of (**c**) Ti, (**d**) Ru, (**e**) O, and (**f**) Zr in $RuZrO_x$/Ti-1.

From Figure 3, distinct lattice fringes can be observed in the $RuZrO_x$/Ti-1 sample. Figure 3g,h clearly show lattice fringes corresponding exclusively to the (110) crystal plane of RuO_2. Notably, due to lattice expansion induced by Zr doping, the interplanar spacing of the (110) plane increases from 0.318 nm to 0.319 nm. Furthermore, local lattice distortion can also be observed in Figure 3b. In the EDS mappings shown in Figure 3c–f, the presence of Zr element is detected in addition to Ru and O. All of the above observations indicate the successful doping of Zr. The XRD patterns of the $RuZrO_x$/Ti-1, $RuZrO_x$/Ti-2, and

RuO_x/Ti catalyst samples are presented in Figure 4a. Due to the strong diffraction peaks of the Ti substrate and the significant overlap between the peak positions of Ti (PDF#44-1294) and RuO_2 (PDF#40-1290), it is extremely difficult to observe characteristic peaks attributable to ruthenium oxide in the XRD patterns of the $RuZrO_x$/Ti-1 and RuO_x/Ti samples calcined under a N_2 atmosphere [27]. The diffraction peak s located at 35°, 38°, 40°, 53°, 63°, 71°, 76°, 77°, 82°, 87°, and 93° can all be attributed to Ti, corresponding to its (100), (002), (101), (102), (110), (103), (112), (201), (004), (202), and (104) crystal planes, respectively. The diffraction peaks at 35°, 40°, 77°, and 93° are overlapping peaks of Ru_2 and Ti, assignable to the (101), (111), (212), and (330) crystal planes of RuO_2, respectively. Furthermore, by observing the $RuZrO_x$/Ti-2 sample calcined in an air atmosphere, characteristic peaks corresponding to the (110) and (211) crystal planes of RuO_2 can be discerned at 28° and 54°. This suggests that the catalyst sample calcined under a N_2 atmosphere was not fully oxidized, resulting in a relatively low RuO_2 content.

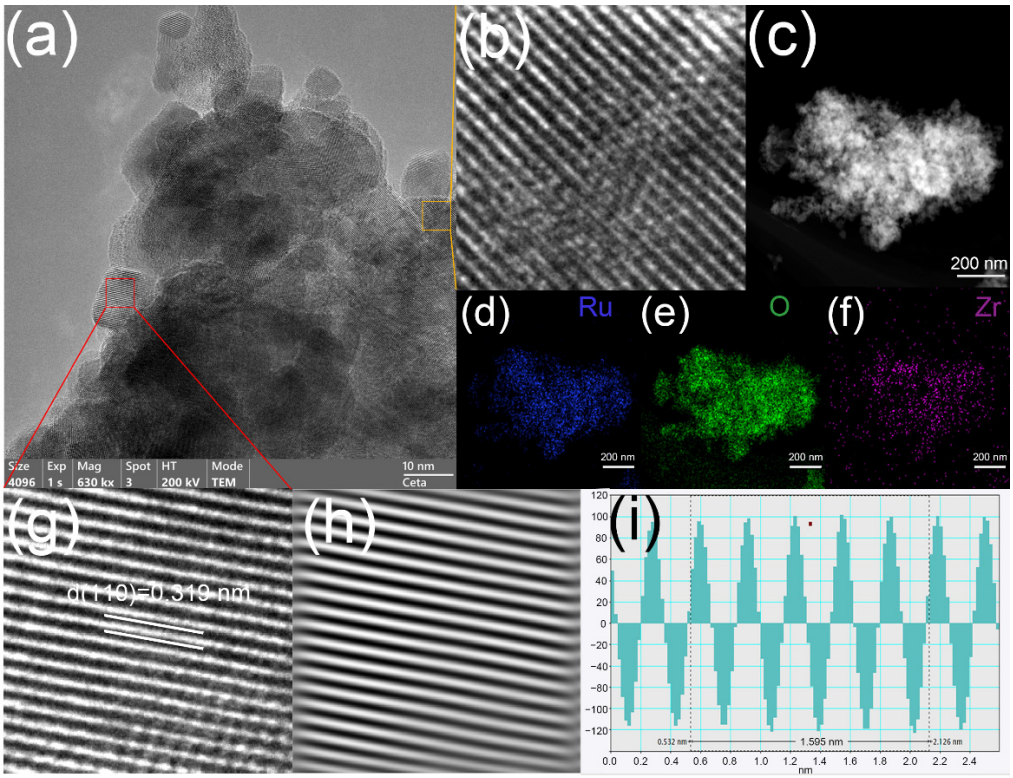

Figure 3. (**a**) HRTEM image of $RuZrO_x$/Ti-1; (**b**) Enlarged view of the lattice fringe region in the yellow area; (**c**–**f**) TEM image and EDS mapping of RuZrOx/Ti-1; (**g**) Enlarged view of the lattice fringe region in the red area; (**h**) Inverse Fourier transform lattice fringe image; (**i**) Lattice spacing analysis diagram.

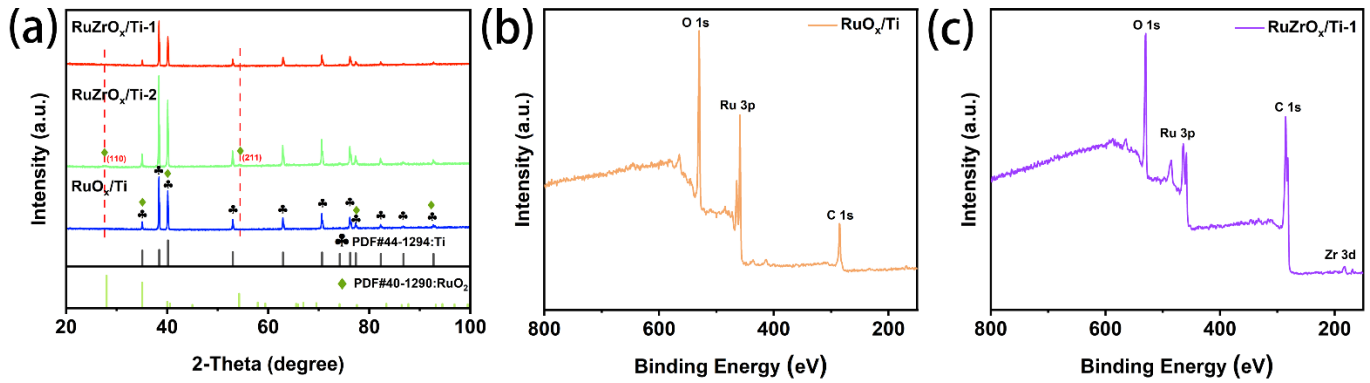

Figure 4. (**a**) XRD patterns of $RuZrO_x$/Ti-1, $RuZrO_x$/Ti-2, and RuO_x/Ti; (**b**) XPS survey spectrum of RuO_x/Ti; (**c**) XPS survey spectrum of $RuZrO_x$/Ti-1.

Due to the excessively strong diffraction peaks originating from the Ti substrate, the interpretability of the XRD patterns regarding the phase composition of the as-prepared material is compromised. To further verify the successful synthesis of the catalyst material, X-ray photoelectron spectroscopy (XPS) was employed to investigate the chemical composition and elemental valence states of the catalyst samples. The survey spectra shown in Figure 4b,c reveal the presence of Ru, Zr, and Ti elements in the $RuZrO_x$/Ti-1 sample, confirming the successful introduction of Zr into the catalyst. In contrast, the RuO_x/Ti sample contains only Ru and Ti. Figure 5a displays the high-resolution Ru 3d spectrum, which comprises three main peaks and one satellite peak [29]. Specifically, the peaks at binding energies of 280.8 eV, 282.3 eV, and 283.3 eV correspond to Ru^{4+}, Ru^{3+}, and a satellite peak, respectively. Due to the close proximity of the binding energy of the carbon peak (C 1s) to that of the Ru peaks in the Ru 3d region, a main C peak is also observable at 284.7 eV in the Ru 3d spectrum. The high-resolution Ru 3p spectrum is shown in Figure 5b. In the RuO_x/Ti sample, peaks for Ru^{4+} and Ru^{3+} are located at 462 eV and 464 eV, respectively, while a satellite peak is observed at 466.7 eV. Notably, compared to the Ru 3p spectrum of the RuO_x/Ti sample, the characteristic Ru peaks for the $RuZrO_x$/Ti-1 sample shift towards higher binding energies. The peaks for Ru^{4+} and Ru^{3+} are observed at 463 eV and 464.5 eV, respectively [30]. This phenomenon indicates a lower oxidation state of Ru in RuZrOx-1 compared to RuO_x/Ti, demonstrating that electron transfer from Zr to Ru occurs upon doping with the less electronegative Zr. This promotes the formation of lower-valence Ru and increases its proportion, which is beneficial for enhancing the catalytic activity and stability of the catalyst [11,27]. Additionally, due to the spectral overlap between the Ti 2p and Ru 3p regions, a peak attributable to Ti can be observed at 458.5 eV in the high-resolution Ru 3p spectrum [31]. The position of this Ti peak remains consistent and is unaffected by Zr doping.

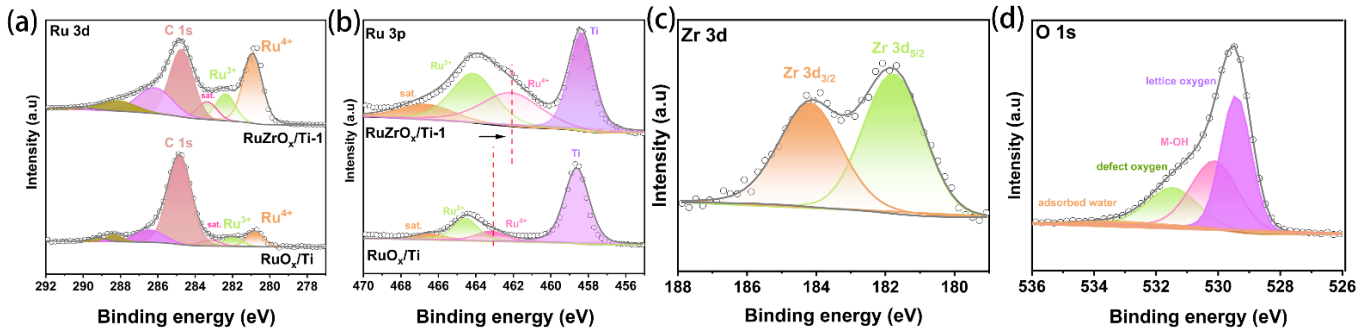

Figure 5. XP spectra of (**a**) $RuZrO_x$/Ti-1 and RuO_x/Ti: Ru 3d; (**b**) $RuZrO_x$/Ti-1 and RuO_x/Ti: Ru 3p; (**c**) $RuZrO_x$/Ti-1: Zr 3d; (**d**) $RuZrO_x$/Ti-1: O 1s.

The high-resolution Zr 3d spectrum is presented in Figure 5c. Two distinct peaks are observed at binding energies of 181.7 eV and 184.2 eV, corresponding to Zr 3d5$_{5/2}$ and Zr 3d3$_{3/2}$, respectively [32]. The detection of clear Zr characteristic peaks in the XPS spectrum provides direct evidence for the successful doping of Zr. Finally, the high-resolution O 1s spectrum is displayed in Figure 5d. Characteristic peaks corresponding to adsorbed water, oxygen vacancies, –OH species, and lattice oxygen are located at 533.3 eV, 531.5 eV, 530 eV, and 529.4 eV, respectively. The presence of oxygen vacancies is conducive to the improvement of the catalyst's performance. First, oxygen vacancies alter the local coordination environment and electronic density of states around the Ru active sites. The characteristic peaks in the Ru 3p XPS spectrum shift toward higher binding energies, indicating a reduction in the oxidation state of Ru and effective suppression of Ru overoxidation and dissolution. On the other hand, oxygen vacancies are conducive to triggering the lattice oxygen oxidation mechanism (LOM), which directly bypasses the high-energy-barrier step of *OOH formation [33–36]. The detection of Ru, Zr, O, and Ti in the XPS analysis corroborates the results obtained from the energy-dispersive X-ray spectroscopy (EDS) mapping under scanning electron microscopy.

As shown in the LSV curves of different samples in Figure 6a, $RuZrO_x$/Ti-1 exhibits superior OER performance compared to $RuZrO_x$/Ti-2, RuO_x/Ti, and the bare Ti mesh. The overpotentials of the four samples at a current density of 10 mA·cm^{-2} are presented in Figure 6b, which are 199 mV ($RuZrO_x$/Ti-1), 254 mV ($RuZrO_x$/Ti-2), 382 mV (RuO_x/Ti), and 742 mV (Ti), respectively. The sufficiently high overpotential is sufficient to prove that the Ti mesh exists merely as a substrate and has a negligible contribution to the catalyst performance (The comparison of overpotentials and Tafel slopes of the RuZrOx/Ti-1 catalyst with those of other similar catalysts reported in recent years is presented in Table S1) [37–40]. Among these, $RuZrO_x$/Ti-1 displays the lowest overpotential, demonstrating the optimal OER activity. This enhancement can be attributed to the dense nanosphere structure and abundant void spaces on the surface of the $RuZrO_x$/Ti-1 catalyst, which increase the number of accessible active sites. Previous studies have indicated that a larger double-layer capacitance (C_{dl}) value signifies greater exposure of active sites during the electrocatalytic process, leading to correspondingly higher catalytic activity. As shown in the CV curves of $RuZrO_x$/Ti-1 at different scan rates (Figure 6d) and the corresponding linear fit for C_{dl} determination (Figure 6e), the as-prepared $RuZrO_x$/Ti-1 catalyst exhibits a C_{dl} value of 19.7 mF·cm^{-2}. This relatively high double-layer capacitance is indicative of a larger electrochemically active surface area.

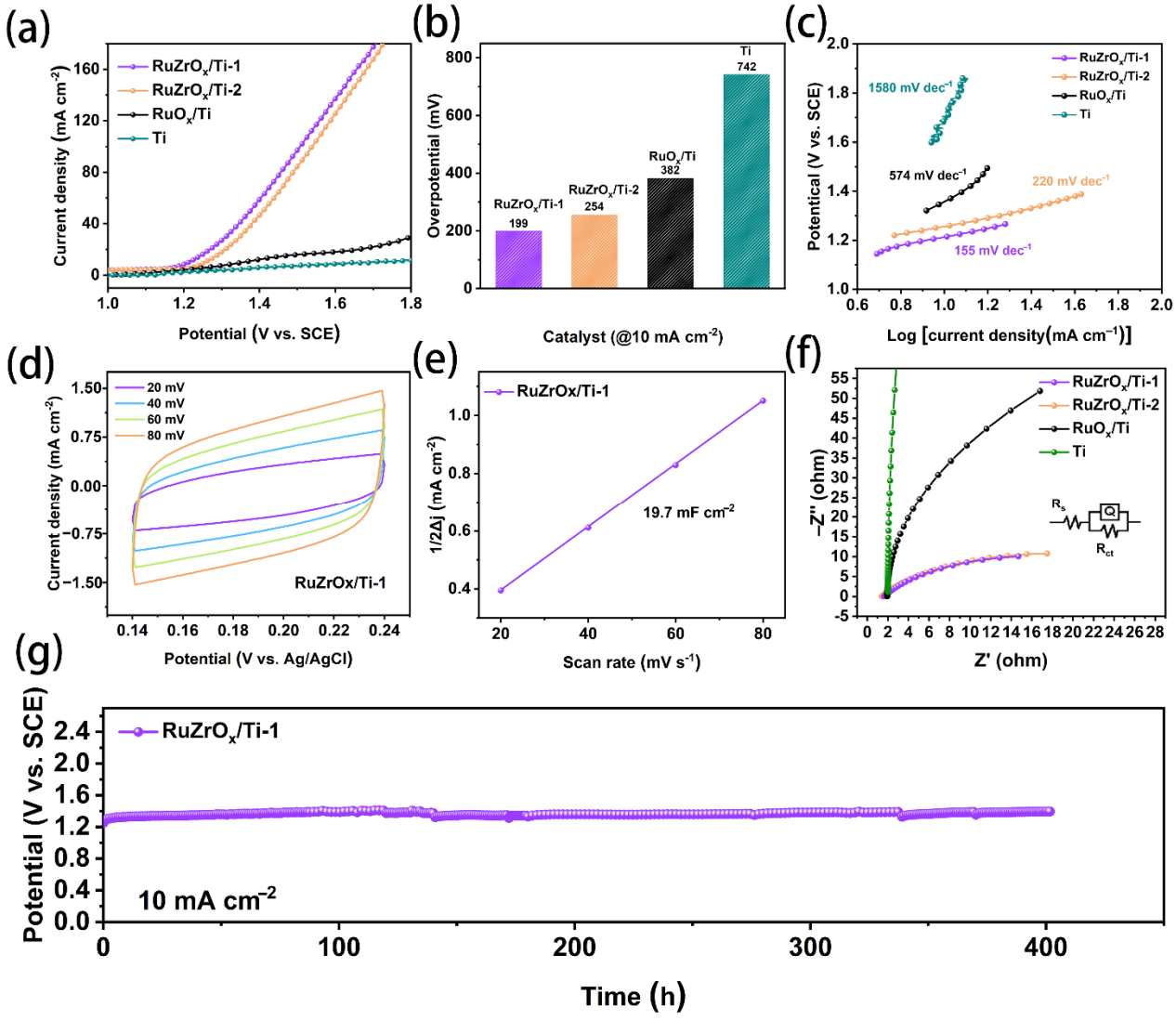

Figure 6. (**a**) LSV curves of different catalysts; (**b**) Overpotential values of different catalysts at a current density of 10 mA·cm^{-2}; (**c**) Tafel plots of different catalysts; (**d**) CV curves of $RuZrO^x$/Ti-1 in the non-Faradaic region at various scan rates; (**e**) C_{dl} fitting plots of $RuZrO^x$/Ti-1; (**f**) EIS Nyquist plots of different catalysts; (**g**) Chronopotentiometry curve of $RuZrO_x$/Ti-1 at a constant current density of 10 mA·cm^{-2}.

The differences in reaction kinetics among the various catalyst samples were compared using Tafel slopes and electrochemical impedance spectroscopy. Studies have demonstrated that a smaller Tafel slope corresponds to faster reaction kinetics. As observed in the Tafel slope comparison of different samples in Figure 6c, the $RuZrO_x$/Ti-1 catalyst exhibits the smallest Tafel slope of 155 $mV \cdot dec^{-1}$. In contrast, the Tafel slopes for the $RuZrO_x$/Ti-2 catalyst, RuO_x/Ti catalyst, and bare Ti mesh are 220 $mV \cdot dec^{-1}$, 574 $mV \cdot dec^{-1}$, and 1580 $mV \cdot dec^{-1}$, respectively, all higher than that of $RuZrO_x$/Ti-1. The electrochemical impedance spectroscopy (EIS) results in Figure 6f further corroborate the faster reaction kinetics of the $RuZrO_x$/Ti-1 catalyst, which displays a charge transfer resistance of 19 Ω, lower than that of $RuZrO_x$/Ti-2 (23 Ω) and RuO_x/Ti (245 Ω). This indicates that the $RuZrO_x$/Ti-1 catalyst possesses a faster electron transfer rate during the OER process, thereby contributing to its enhanced catalytic performance.

In addition to catalytic activity, the stability of a catalyst is another crucial parameter for evaluating its overall performance. The chronoamperometry curve for the $RuZrO_x$/Ti-1 catalyst was recorded at a fixed current density of 10 $mA \cdot cm^{-2}$. The results, shown in Figure 6g, demonstrate that the sample remains stable over 400 h without any significant decay. After the stability test, the potential increased by only 6.9%, indicating that the $RuZrO_x$/Ti-1 catalyst exhibits excellent long-term stability. To verify the structural integrity of the $RuZrO_x$/Ti-1 catalyst after the stability test, a fresh XPS analysis was performed. The results are shown in Figures S3–S5. It can be observed that the XPS spectrum of the Ru 3d region displays the same features as those of the sample before the stability test, indicating that no significant dissolution or loss of Ru occurred during the stability test. Due to the low amount of Zr as a dopant and the prolonged stability test, the XPS signals in the Zr 3d region are relatively weak; nevertheless, the characteristic peaks corresponding to Zr $3d_{3/2}$ and Zr $3d_{5/2}$ can still be discerned. The O 1s XPS spectrum reveals that the Ru–OH peak of $RuZrO_x$/Ti-1 becomes stronger, which is a result of surface hydroxylation, indicating the formation of a stable active layer on the sample surface.

Moreover, *in-situ* Raman spectroscopy was employed to monitor the changes occurring in the catalysts during the OER. The *in-situ* Raman spectra of the $RuZrO_x$/Ti-1 catalyst and the RuO_x/Ti catalyst are shown in Figure 7a,b, respectively. In the Raman spectra of both samples at open circuit potential, four characteristic peaks attributable to RuO_2 can be observed. Specifically, the characteristic peaks located at 419 cm^{-1} and 516 cm^{-1} are assigned to the Eg vibration modes of RuO_2, while the peaks at 604 cm^{-1} and 696 cm^{-1} correspond to the A1g and B2g vibration modes of RuO_2, respectively [11,41–43]. It is worth noting that as the potential increases, the configuration of the Ru–O bonds in $RuZrO_x$/Ti-1 remains stable, exhibiting neither a red shift nor a blue shift with increasing voltage, which serves as evidence for its excellent stability. In contrast, for the RuO_x/Ti catalyst, as the potential increases, a significant overall red shift of the characteristic peaks at 419 cm^{-1} and 604 cm^{-1} can be clearly observed (from 419 cm^{-1} to 410 cm^{-1}; from 604 cm^{-1} to 599 cm^{-1}). This indicates that the Ru–O bond length begins to contract during the OER process, which is detrimental to maintaining the stability of the catalyst.

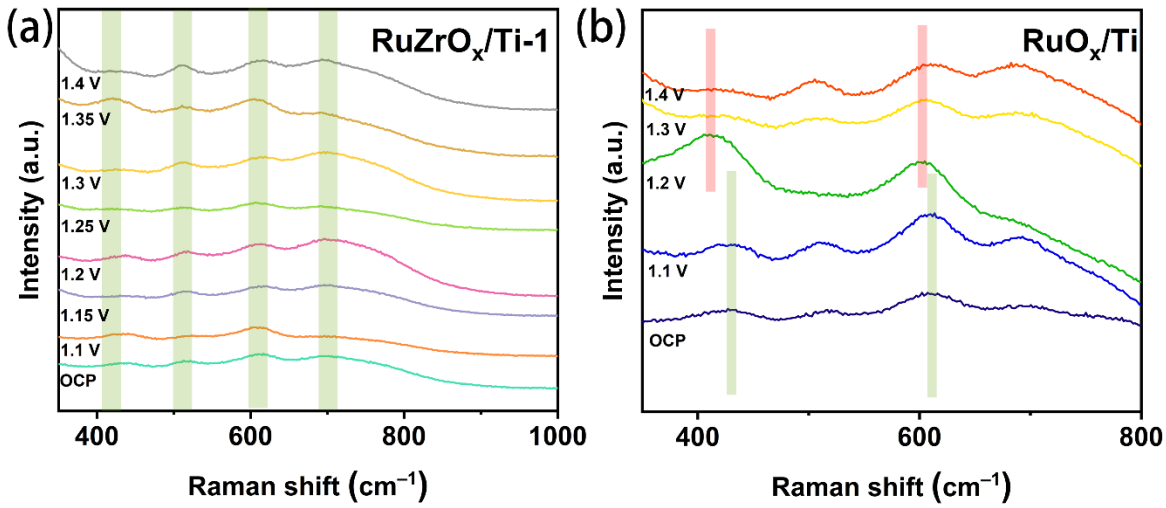

Figure 7. (**a**) *In-situ* Raman spectra of RuZrO$_x$/Ti-1 at different potentials; (**b**) *In-situ* Raman spectra of RuO$_x$/Ti at different potentials.

4. Conclusions

In this study, a promising RuZrO$_x$/Ti composite catalyst for acidic oxygen evolution was successfully fabricated via a drop-coating and one-step pyrolysis process. The catalyst surface exhibits a densely packed nanosphere morphology accompanied by abundant pore structures. The introduction of the metallic element Zr effectively modulated the molecular structure within the catalyst, optimizing the adsorption behavior of reaction intermediates during the OER in acidic media. This modulation not only lowers the reaction energy barrier but also inhibits the overoxidation of Ru, effectively suppressing the irreversible dissolution of Ru and the loss of lattice oxygen. The RuZrO$_x$/Ti catalyst achieves a low overpotential of only 199 mV at a current density of 10 mA·cm^{-2} for the OER. Furthermore, it demonstrates exceptional long-term durability, operating stably for 400 h at a fixed current density of 10 mA·cm^{-2}. In summary, this work provides a viable strategy for designing high-performance acidic OER catalysts, thereby paving the way for the advancement of electrodes for water oxidation.

Supplementary Materials

The following supporting information can be found at: https://www.sciepublish.com/article/pii/973, Figure S1: LSV curves at different molar ratios. Figure S2: Particle size distribution graph. Figure S3: XPS spectra of the Ru 3d orbitals after the stability test. Figure S4: XPS spectra of the Zr 3d orbitals after the stability test. Figure S5: XPS spectra of the O 1s orbitals after the stability test. Table S1: Specific capacitance and corresponding current density of various materials.

Statement of the Use of Generative AI and AI-Assisted Technologies in the Writing Process

During the preparation of this manuscript, the author(s) used [Deepseek] in order to [make the sentence more fluent and standardized]. After using this tool/service, the author(s) reviewed and edited the content as needed and take(s) full responsibility for the content of the published article.

Acknowledgments

The authors appreciate the financial support from the National Natural Science Foundation of (China No. 52574436), the Industrial Innovation Talent Special Project of Yunnan Province's Xingdian Talent Support Plan (No. yfgrc202417).

Author Contributions

Investigation, J.Z. and X.W.; Resources, R.X.; Data Curation, J.Z.; Writing—Original Draft Preparation, J.Z.; Writing—Review & Editing, X.W.; Visualization, J.Z.; Supervision, X.W.; Project Administration, R.X.; Funding Acquisition, R.X.; Funding Acquisition, J.W.

Ethics Statement

Not applicable.

Informed Consent Statement

Not applicable.

Data Availability Statement

The data that support the findings of this study are available from the corresponding author, [Prof. Xu, rdxupaper@aliyun.com], upon reasonable request.

Funding

The authors appreciate the financial support from National Natural Science Foundation of China (No. 52574436), The Industrial Innovation Talent Special Project of Yunnan Province's Xingdian Talent Support Plan (No. yfgrc202417), and the Yunnan Fundamental Research Projects (Grant No. 202301AT070399).

Declaration of Competing Interest

The authors declare that they have no known competing financial interests or personal relationships that could have appeared to influence the work reported in this paper.

References

1. Jiao J, Chen D, Zhao H, Dong Y, Mu S. Durable ruthenium oxide catalysts for water oxidation reaction. *Sci. China Chem.* **2025**, *68*, 2217–2233. DOI:10.1007/s11426-024-2227-2
2. Xu H-M, Zhu H-R, Huang C-J, Zhang Z-J, Shuai T-Y, Zhan Q-N, et al. Recent advances in Fe-N-C- and Co-N-C-based materials as bifunctional electrocatalysts for oxygen reduction and oxygen evolution. *Sci. China Chem.* **2024**, *67*, 1137–1160. DOI:10.1007/s11426-023-1863-8
3. Tockhorn P, Sutter J, Cruz A, Wagner P, Jäger K, Yoo D, et al. Nano-optical designs for high-efficiency monolithic perovskite–silicon tandem solar cells. *Nat. Nanotechnol.* **2022**, *17*, 1214–1221. DOI:10.1038/s41565-022-01228-8
4. Zhao S, Yang Y, Tang Z. Insight into Structural Evolution, Active Sites, and Stability of Heterogeneous Electrocatalysts. *Angew. Chem. Int. Ed.* **2022**, *61*, e202110186. DOI:10.1002/anie.202110186
5. Yang Y, Gao H, Zhu C, Sun W, Zeng J, Wang X, et al. Enriching Edge-Structures of NiFe-LDH via Ru–Ni Site Interchange as Efficient and Stable OER Catalytic Electrodes. *Adv. Funct. Mater.* **2026**, *36*, e14599. DOI:10.1002/adfm.202514599
6. Aboelazm E, Thalji MR, Hamid MA, Park H, Zuhaib H, Khe CS, et al. d–p–d orbital coupling-driven electronic modulation in $CoSe_2/TiSe_2@Ti_3C_2T_x$ MXene for enhanced supercapacitors and oxygen evolution reaction. *Chem. Eng. J.* **2026**, *528*, 172358. DOI:10.1016/j.cej.2025.172358
7. Wang E, Luo L, Feng Y, Wu A, Li H, Luo X, et al. Ultrafine ordered $L1_2$-Pt–Co–Mn ternary intermetallic nanoparticles as high-performance oxygen-reduction electrocatalysts for practical fuel cells. *J. Energy Chem.* **2024**, *93*, 157–165. DOI:10.1016/j.jechem.2024.01.054
8. Zhao W, Chi B, Liang L, Yang P, Zhang W, Ge X, et al. Optimizing the Electronic Structure of Ordered Pt–Co–Ti Ternary Intermetallic Catalyst to Boost Acidic Oxygen Reduction. *ACS Catal.* **2022**, *12*, 7571–7578. DOI:10.1021/acscatal.2c00554
9. She L, Zhao G, Ma T, Chen J, Sun W, Pan H. On the Durability of Iridium-Based Electrocatalysts toward the Oxygen Evolution Reaction under Acid Environment. *Adv. Funct. Mater.* **2022**, *32*, 2108465. DOI:10.1002/adfm.202108465

10. Liu M, Zhang Y-Q, Wang X, Lang F, Li N, Bu X-H. Recent advances in metal-organic frameworks for oxygen evolution reaction electrocatalysts. *Sci. China Chem.* **2023**, *66*, 2754–2779. DOI:10.1007/s11426-023-1725-8
11. Zhou D, Chang Y, Tang J, Ou P. $Mn_{0.75}Ru_{0.25}O_2$ with Low Ru Concentration for Active and Durable Acidic Oxygen Evolution. *Small* **2025**, *21*, 2412265. DOI:10.1002/smll.202412265
12. Cherevko S, Geiger S, Kasian O, Kulyk N, Grote J-P, Savan A, et al. Oxygen and hydrogen evolution reactions on Ru, RuO_2, Ir, and IrO_2 thin film electrodes in acidic and alkaline electrolytes: A comparative study on activity and stability. *Catal. Today* **2016**, *262*, 170–180. DOI:10.1016/j.cattod.2015.08.014
13. Ying J, Chen J-B, Xiao Y-X, Cordoba de Torresi SI, Ozoemena KI, Yang X-Y. Recent advances in Ru-based electrocatalysts for oxygen evolution reaction. *J. Mater. Chem. A* **2023**, *11*, 1634–1650. DOI:10.1039/D2TA07196G
14. Xu X, Jo YH, Yu T. Facile synthesis of ultra-small Ru/NiO hybrid nanoparticles anchored on carbon nanotubes for enhanced bifunctional OER and HER performance. *Int. J. Hydrogen Energy* **2026**, *208*, 153543. DOI:10.1016/j.ijhydene.2026.153543
15. Yang W, Jia L, Cao J, Miao Y, Mei B, Ouyang R, et al. Lanthanides Regulate the Oxide Pathway Mechanism of RuO_2 to Boost Acidic Oxygen Evolution. *Nano Lett.* **2026**, *26*, 3873–3881. DOI:10.1021/acs.nanolett.6c00082
16. Wang J, Cheng C, Yuan Q, Yang H, Meng F, Zhang Q, et al. Exceptionally active and stable RuO_2 with interstitial carbon for water oxidation in acid. *Chem* **2022**, *8*, 1673–1687. DOI:10.1016/j.chempr.2022.02.003
17. Chang J, Shi Y, Wu H, Yu J, Jing W, Wang S, et al. Oxygen Radical Coupling on Short-Range Ordered Ru Atom Arrays Enables Exceptional Activity and Stability for Acidic Water Oxidation. *J. Am. Chem. Soc.* **2024**, *146*, 12958–12968. DOI:10.1021/jacs.3c13248
18. Wang J, Yang H, Li F, Li L, Wu J, Liu S, et al. Single-site Pt-doped RuO_2 hollow nanospheres with interstitial C for high-performance acidic overall water splitting. *Sci. Adv.* **2022**, *8*, eabl9271. DOI:10.1126/sciadv.abl9271
19. Zhang D, Li M, Yong X, Song H, Waterhouse GIN, Yi Y, et al. Construction of Zn-doped RuO_2 nanowires for efficient and stable water oxidation in acidic media. *Nat. Commun.* **2023**, *14*, 2517. DOI:10.1038/s41467-023-38213-1
20. Wei D, Liu TM, He YH, Wei BY, Pan JH, Zhang JW, et al. Corrigendum: Radical 1,4/5-Amino Shift Enables Access to Fluoroalkyl-Containing Primary β(γ)-Aminoketones under Metal-Free Conditions. *Angew. Chem. Int. Ed.* **2021**, *60*, 26020. DOI:10.1002/anie.202114499
21. Ospina-Acevedo F, Albiter LA, Bailey KO, Godínez-Salomón JF, Rhodes CP, Balbuena PB. Catalytic Activity and Electrochemical Stability of $Ru_{1-x}M_xO_2$ (M = Zr, Nb, Ta): Computational and Experimental Study of the Oxygen Evolution Reaction. *ACS Appl. Mater. Interfaces* **2024**, *16*, 16373–16398. DOI:10.1021/acsami.4c01408
22. Zhang H-Z, Wang X, Xie Y-F, Li C, Zhao Z-G, Shao P-Y, et al. Weakening the RuO covalency to promote the dominance of adsorbate evolution mechanism pathway by zirconium doping for ultra-stable proton exchange membrane water electrolysis. *J. Colloid Interface Sci.* **2026**, *703*, 139091. DOI:10.1016/j.jcis.2025.139091
23. Wang W, Li Y, Wang J, Xiao R, Liu K, Song X, et al. Interfacial electron redistribution through the Ru–N–Fe bond to stabilize high-valence metal sites for efficient electrocatalytic oxygen evolution. *Renew. Energy* **2025**, *244*, 122656. DOI:10.1016/j.renene.2025.122656
24. Bayatsarmadi B, Zheng Y, Tang Y, Jaroniec M, Qiao S-Z. Significant Enhancement of Water Splitting Activity of N-Carbon Electrocatalyst by Trace Level Co Doping. *Small* **2016**, *12*, 3703–3711. DOI:10.1002/smll.201601131
25. Abdul M, Jiang X, Alotaibi NH, Mohammad S, Rahman AU, Jing B, et al. Synergistic improvement of OER/HER electrocatalytic performance of Cu_2Te via the introduction of Zr for water electrolysis. *Int. J. Hydrogen Energy* **2025**, *128*, 329–341. DOI:10.1016/j.ijhydene.2025.04.259
26. Huang Y, Zhou T, Hu Y, Yang Y, Yang F, Huang W, et al. Ordered derivatives on Ti surface enhance the OER activity and stability of Ru-based film electrode. *Int. J. Hydrogen Energy* **2023**, *48*, 33411–33421. DOI:10.1016/j.ijhydene.2023.05.108
27. Zhang X-Y, Yin H, Dang C-C, Nie H, Huang Z-X, Zheng S-H, et al. Unlocking Enhanced Catalysis Stability in Acidic Oxygen Evolution: Structural Insights for PEM Applications under High-Current Density. *Angew. Chem. Int. Ed.* **2025**, *64*, e202425569. DOI:10.1002/anie.202425569
28. Wang X, Wang J, Xu R, Yang L. Boosting the electrocatalytic performance of Co_2P/Ni_3S_2 heterostructure for efficient water splitting. *Int. J. Hydrogen Energy* **2024**, *91*, 683–692. DOI:10.1016/j.ijhydene.2024.10.205
29. Xu N, Li M-M, Sun H-Y, Li G, Wen X, Ouyang D, et al. Atmosphere-driven oriental regulation of Ru valence for boosting alkaline water electrolysis. *Chem. Eng. J.* **2024**, *502*, 158051. DOI:10.1016/j.cej.2024.158051
30. Zhou F, Chen J, Yang Y, Ke X, Liu X, Zhang L, et al. Exceptionally active and stable RuO_2 by constructing p-n heterojunction between Co_3O_4 and RuO_2 for acidic water oxidation. *Appl. Surf. Sci.* **2023**, *641*, 158508. DOI:10.1016/j.apsusc.2023.158508

31. Wang G, Wan W, Chen M, Li J, Wu X, Huang S, et al. Building strong metal-support interaction between TiN and RuO_2 for efficient acidic oxygen evolution reaction. *Int. J. Hydrogen Energy* **2024**, *71*, 804–810. DOI:10.1016/j.ijhydene.2024.05.315
32. Yang G, Zhu B, Fu Y, Zhao J, Lin Y, Gao D, et al. High-valent Zirconium-doping modified Co_3O_4 weave-like nanoarray boosts oxygen evolution reaction. *J. Alloys Compd.* **2021**, *886*, 161172. DOI:10.1016/j.jallcom.2021.161172
33. Bao J, Zhang X, Fan B, Zhang J, Zhou M, Yang W, et al. Ultrathin Spinel-Structured Nanosheets Rich in Oxygen Deficiencies for Enhanced Electrocatalytic Water Oxidation. *Angew. Chem. Int. Ed.* **2015**, *54*, 7399–7404. DOI:10.1002/anie.201502226
34. Gao J, Xu C-Q, Hung S-F, Liu W, Cai W, Zeng Z, et al. Breaking Long-Range Order in Iridium Oxide by Alkali Ion for Efficient Water Oxidation. *J. Am. Chem. Soc.* **2019**, *141*, 3014–3023. DOI:10.1021/jacs.8b11456
35. Xiao PW, Zhang ZF, Ge JJ, Deng YL, Chen XF, Zhang JR, et al. Surface passivation of intensely luminescent all-inorganic nanocrystals and their direct optical patterning. *Nat. Commun.* **2023**, *14*, 49. DOI:10.1038/s41467-022-35702-7
36. Sun L, Feng M, Peng Y, Zhao X, Shao Y, Yue X, et al. Constructing oxygen vacancies by doping Mo into spinel Co_3O_4 to trigger a fast oxide path mechanism for acidic oxygen evolution reaction. *J. Mater. Chem. A* **2024**, *12*, 8796–8804. DOI:10.1039/D4TA00655K
37. Wang H, Wen T, Gong X, Ren M, Tang Q, Hu A, et al. Ta-doped charge-transferring Ir shells on Ru cores: Dual stabilisation and synergistic OER catalysis for PEMWE. *Chem. Commun.* **2026**, *62*, 6586–6590. DOI:10.1039/D6CC00726K
38. Li L, Zhao J, Song Y, Li C, Zeng X, Chen L, et al. Synthesis of highly active oxygen evolution reaction electrocatalysts using balsa woods. *Mater. Lett.* **2024**, *357*, 135744. DOI:10.1016/j.matlet.2023.135744
39. Zhang J, Qin H, Cao X, Jia W, Ma R, Chen X, et al. Constructing Adjustable Heterointerface for Enhancing Acidic Oxygen Evolution Performances of RuO_2@$CoMnO_3$ Nanosheets Electrocatalysts. *ACS Mater. Lett.* **2024**, *6*, 3016–3024. DOI:10.1021/acsmaterialslett.4c00778
40. Yang S, Wang Y, Gong Y. Anchoring ruthenium single atoms into the carbon nanotubes-supported nickel-based sulfides for enhanced electrocatalytic oxygen evolution. *J. Colloid Interface Sci.* **2025**, *699*, 138255. DOI:10.1016/j.jcis.2025.138255
41. Li L, Zhang G, Zhou C, Lv F, Tan Y, Han Y, et al. Lanthanide-regulating Ru-O covalency optimizes acidic oxygen evolution electrocatalysis. *Nat. Commun.* **2024**, *15*, 4974. DOI:10.1038/s41467-024-49281-2
42. Yuan B, Dang Q, Liu H, Sendeku MG, Peng J, Fan Y, et al. Synergistic niobium and manganese co-doping into RuO_2 nanocrystal enables PEM water splitting under high current. *Nat. Commun.* **2025**, *16*, 4583. DOI:10.1038/s41467-025-59710-5
43. Chen Y, Liu Y, Li L, Sakthive T, Guo Z, Dai Z. Asymmetric Bond Delta-Polarization at the Interfacial Se–Ru–O Bridge for Efficient pH-Robust Water Electrolysis. *Adv. Funct. Mater.* **2024**, *34*, 2406587. DOI:10.1002/adfm.202406587